

# Liquid-vapor phase transitions in nuclei: Theoretical approaches and experimental evidence

L. G. Moretto\*, J. B. Elliott\*, L. Phair\* and G. J. Wozniak\*

*\*Nuclear Science Division, Lawrence Berkeley National Laboratory,  
University of California, Berkeley, California 94720*

**Abstract.** The leptodermous approximation is applied to nuclear systems for  $T > 0$ . The introduction of surface corrections leads to anomalous caloric curves and to negative heat capacities in the liquid-gas coexistence region. Clusterization in the vapor is described by associating surface energy to clusters according to Fisher's formula. The three-dimensional Ising model, a leptodermous system par excellence, does obey rigorously Fisher's scaling up to the critical point. Multifragmentation data from several experiments including the ISiS and EOS Collaborations, as well as compound nucleus fragment emission at much lower energy follow the same scaling, thus providing the strongest evidence yet of liquid-vapor coexistence. The phase diagram is obtained for the finite system and an extrapolation is made to infinite nuclear matter.

## INTRODUCTION

Up to now, the nuclear liquid-vapor phase diagram has been based more on educated guesses and artistic license than on experimental fact. We have succeeded in removing this arbitrariness by characterizing the liquid-vapor coexistence curve from low temperatures up to the critical point and in generalizing it to infinite nuclear matter. What follows is an outline of the ideas that have led us to this characterization.

Nuclei are leptodermous, mesoscopic clusters. Their thin skin leads naturally to an expansion of their energy in powers of  $A^{-1/3}$ . The leading term, proportional to the number of nucleons  $A$ , is the bulk term; the second, proportional to  $A^{2/3}$ , is the surface term, the next, proportional to  $A^{1/3}$ , is the curvature term, etc. This is the basis of the liquid drop model, which by merely correcting the bulk terms with a surface term, manages to reproduce the binding energies of nuclei to within 1%. There is reason to believe that a similar leptodermous treatment of nuclear systems at  $T > 0$  should lead to an equivalently good reproduction of nuclear thermodynamical properties.

In particular, the appearance of a vapor phase at  $T > 0$  opens two complementary perspectives for the characterization of phase coexistence: the liquid perspective and the vapor perspective. From the liquid perspective, one is led to consider the transition between a liquid-like nuclear droplet and its equilibrium vapor, with the attendant caloric curve, as well as compound nuclear decay in terms of enthalpy of vaporization. From the vapor perspective one is led to consider the properties of the

vapor phase, especially the extent to which nucleons are aggregated into clusters, as indicators of incipient liquid condensation.

In the first part of this presentation we take the liquid perspective and derive analytically the caloric curve and the (negative) heat capacity for a drop undergoing an isobaric phase transition. In the second part we take the vapor perspective and show that the clusterization in the three-dimensional Ising model can be accounted for in terms of the leptodermous expansion. The rigorous obedience of the mass and temperature scaling law (Fisher's scaling) by the Ising model is exactly paralleled by the nuclear systems in multifragmentation, thus providing the best evidence yet for liquid-vapor coexistence. In particular we shall describe how to generalize the experimental thermodynamical results to the limiting case of infinite nuclear matter. Finally, we revert to the liquid perspective and show how compound nucleus fragment emission can be reconciled with the liquid to vapor phase transition.

## THE ISOBARIC PHASE TRANSITION OF A LIQUID DROP

The thermodynamical equilibrium properties of first order phase transitions are completely describable in terms of the thermodynamic state variables associated with the individual separate phases. For this reason, in contrast with continuous phase transitions, first order phase tran-

sitions are “trivial,” and interesting only in so far as they herald the appearance of a hitherto unknown or undescribed phase.

Renewed attention to phase transitions has been generated by studies of models with well defined Hamiltonians with either short range interactions (e.g. the Ising model [1, 2, 3, 4, 5] or the lattice gas model [6]) or incorporating long range interactions such as gravitation or electro-magnetic interactions. Features expected to disappear in the thermodynamic limit, if such a limit exists, were noticed and were claimed to be essential, characteristic indicators of phase transitions in mesoscopic systems [7]. For instance, first order phase transitions were associated with anomalous convex intruders in the entropy versus energy curves, resulting in back-bendings in the caloric curve, and in negative heat capacities [7].

These anomalies have been attributed to a variety of causes, the foremost of which are surface effects, and long range forces [7]. Unfortunately however, the numerical nature of the calculations tends to make the identification of the causes of negative heat capacities rather problematic.

In the context of nuclear physics, microcanonical models of nuclear multifragmentation have associated the anomalies of a convex intruder with the onset of multifragmentation [7]. Furthermore, lattice gas models in the isobaric regime have also shown negative specific heats in the coexistence region, where multifragmentation also appears [6]. The question of whether the two transitions are related and possibly coincident with the liquid-vapor transition is still very much open.

Recently, the claim has been made of an empirical observation of these anomalies, such as negative heat capacities in nuclear systems [8]. These negative heat capacities have been inferred from the study of fluctuations in multifragmenting nuclear systems. It would be highly desirable to ground any evidence for these anomalies, theoretical or otherwise, on thermodynamics itself, minimally modified to allow for the possible role of surface effects related to the finiteness of the system.

In this section we illustrate analytically how effects such as negative heat capacities can arise within a standard thermodynamic treatment. We consider the evaporation of a drop of ordinary liquid. Our only concern with mesoscopicity is the explicit treatment of the surface of the drop.

No qualitative difference in the picture results by considering a drop of finite radius  $r$ . The only difference is that the overall free energy of the drop as we shall see below, is higher than that of the bulk and the equilibrium vapor pressure is correspondingly higher.

The state of equilibrium between a liquid and its vapor can be described in the simplest way by the Clapeyron

Equation

$$\frac{dp}{dT} = \frac{\Delta H_m}{\Delta V_m T} : \quad (1)$$

here  $p$  and  $T$  are the pressure and temperature,  $\Delta H_m$  is the molar enthalpy of vaporization and  $\Delta V_m$  is the difference of the molar volumes of vapor  $V_m^v$  and liquid,  $V_m^l$ .

Specialization to the case of a drop of radius  $r$  can be achieved by modifying the enthalpy to account for the surface energy [9]

$$\Delta H_m = \Delta H_m^0 - c_s S_m^l = \Delta H_m^0 - \frac{3c_s V_m^l}{r} \quad (2)$$

where  $\Delta H_m^0$  is the “bulk” molar enthalpy,  $S_m^l$  and  $V_m^l$  are the surface and volume of the drop and  $c_s$  is the surface energy coefficient.

Neglecting  $V_m^l$  compared to  $V_m^v$  and considering the vapor ideal, i.e.  $V_m^v = T/p$ , we can integrate Eq. (1), assuming also  $\Delta H_m$  to be constant. We obtain

$$p = p_0 \exp \left( -\frac{\Delta H_m^0}{T} + \frac{3c_s V_m^l}{rT} \right) \quad (3)$$

or

$$p = p_{\text{bulk}} \exp \left( \frac{3c_s V_m^l}{rT} \right). \quad (4)$$

This equation contains *all* the thermodynamical information necessary to characterize the phase coexistence of the liquid drop of radius  $r$  with its vapor. The salient feature is the rise of the vapor pressure with decreasing radius. Fig. 1 gives a map of the function  $p' = p'(T', r')$ , in terms of the scaled variables

$$p' = \frac{p}{p_0}, \quad T' = \frac{T}{\Delta H_m^0}, \quad r' = \frac{\Delta H_m^0}{3c_s V_m^l} r. \quad (5)$$

For any given radius  $r$ , the function  $p = p(T, r)$  describes the equilibrium condition between the drop and its vapor. In other words, it is the phase diagram of the drop.

Let us now introduce some history and construct a caloric curve for a drop of radius  $r_0$  at constant pressure  $p_0$ . As the drop is heated, and before the vapor can appear, the temperature increases according to  $\Delta H = C_p^l \Delta T$ , with  $C_p^l$  is the liquid’s heat capacity and is approximately constant. When  $T$  reaches the value  $T_0$  at which the vapor pressure  $p(r_0) = p_0$ , the vapor first appears and it expands against the container. The heat of vaporization is absorbed at a rate  $H_m(r_0)$ . However, as it evaporates, the drop sees its radius decreasing from its initial value, chosen to be  $r_0' = 5.35$ . At constant temperature the vapor pressure would rise, but, at constant pressure, as we are now operating, the temperature *decreases* as shown in Fig. 1, as the system absorbs its heat of vaporization, so that,

$$\Delta H = \int_r^{r_0} \Delta H_m \frac{dV}{V_m^l} = \frac{4\pi}{V_m^l} \left( \frac{3c_s V_m^l}{\Delta H_m^0} \right)^3 \quad (6)$$

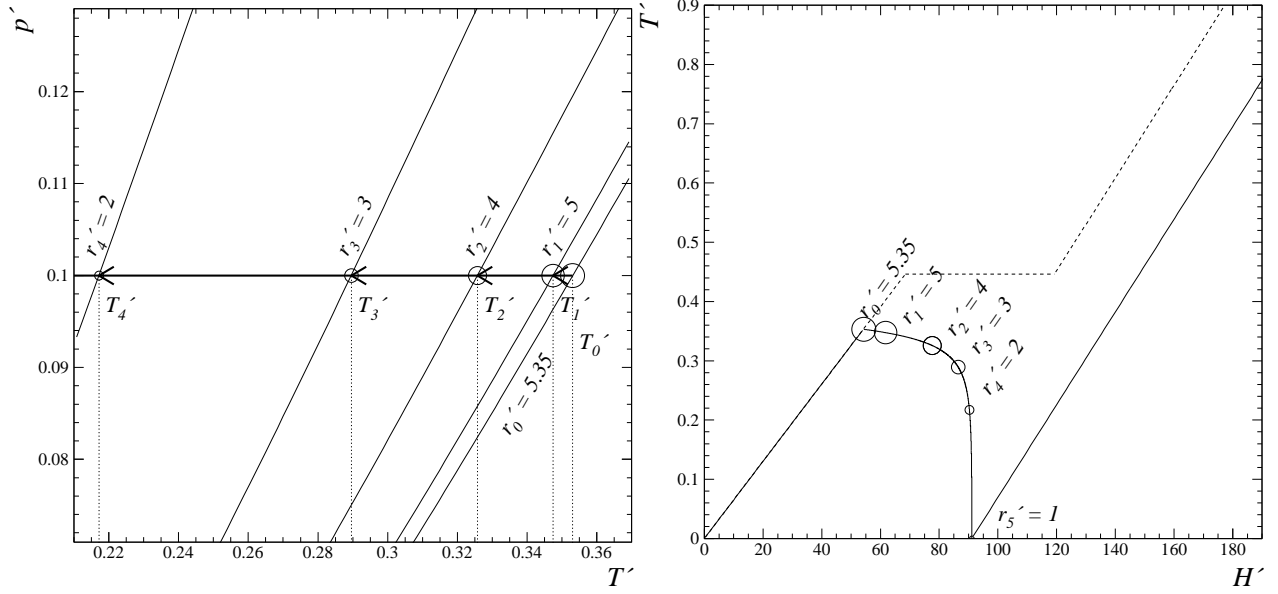


**FIGURE 1.** Left: Saturated vapor pressure as a function of the temperature for different droplet radii. The size of the open circles is proportional to the droplet radius. Right: The history dependent caloric curve of an evaporating drop at constant pressure. Dashed lines represent bulk behavior, solid line shows the drop's caloric curve. The scaled enthalpy is  $H' = H(\Delta H_m^0/3c_s V_m^l)^3/(4\pi/V_m^l)$ .

$$\left[ \frac{1}{3}(r_0'^3 - r'^3) - \frac{1}{2}(r_0'^2 - r'^2) \right]$$

and

$$T' = T_0' \left( \frac{1 - \frac{1}{r'}}{1 - \frac{1}{r_0'}} \right). \quad (7)$$

After the drop has totally evaporated, the vapor can increase its temperature according to  $\Delta H = C_p^v \Delta T$  where  $C_p^v$  is the vapor heat capacity at constant pressure. The resulting caloric curve defined parametrically by Eq. (7) and Eq. (7) and shown in Fig. 1 is rather interesting. It has a decreasing branch associated with the phase transition, along which the heat capacity is negative!

As an aside we note that the scaled radius  $r'$  is just the ratio of the bulk energy to the surface energy. Thus for a nuclear system the range shown:  $1 \leq r_0' \leq 5.35$ , corresponds to a gold nucleus ( $A = 197$ ) evaporating to a single nucleon.

These rather extraordinary features are wholly due to the interesting but, in a way, accidental history of the decreasing radius with increasing evaporation.

Typically, experiments heat a preassigned system with a certain amount of energy  $\Delta E$  or  $\Delta H$ , and determine the resulting change in entropy  $S$  and temperature  $1/T = \partial S/\partial E|_V$ ; from the resulting caloric curve, phase coexistence diagrams are extracted. However, as shown above, the evolution of the system occurring during heating introduces complications in the construction of a phase diagram from such a caloric curve.

To avoid this problem an experimentalist or theorist would have to keep the radius constant or correct for its change while determining the vapor pressure as a function of the temperature, thereby eliminating the accidental aspects associated with the evolution of the system.

The results obtained here are firmly grounded on thermodynamics with a straightforward accounting of finiteness through the surface correction. They are exact in the limit in which the liquid drop model holds, namely, down to nuclei/clusters containing 20 or so constituents. They are completely general, as they do not depend on specific details of the system but rather on its gross properties. In fact, they should be used as the paragon for lattice gas models and the like. In the limit in which these models represent liquid vapor coexistence, they must reproduce the present results.

*Even more importantly, this approach obviates the need for repeating numerical calculations for each individual system or drop size. All that is required is to determine the bulk energy (enthalpy) and the surface energy coefficient of a given phase once and for all.*

It is worth repeating that, once the constraint of constant pressure is enforced, the results described here are entirely general, as they apply to any small system undergoing solid-vapor or liquid vapor transitions.

# THE THREE-DIMENSIONAL ISING MODEL: A PARADIGM OF LIQUID-VAPOR COEXISTENCE IN NUCLEAR MULTIFRAGMENTATION

Two features associated with the fragment multiplicities are found to be quite pervasive in all multifragmentation reactions. They have been named “reducibility” and “thermal scaling” [9, 10, 11].

Reducibility is the property that the probability of observing  $n$ -fragments of a given size is expressible in terms of an elementary one-fragment probability. This property can occur only if fragments are independent of one another and it coincides with stochasticity. Both binomial, and its limiting form, Poissonian reducibilities have been extensively documented experimentally for nuclear multifragmentation [9, 10, 11].

Thermal scaling is the linear dependence of the logarithm of the one-fragment probability with  $1/T$  (an Arrhenius plot). It indicates that the emission probability for fragment type  $i$  has a Boltzmann dependence

$$q_i = q_0 e^{-B_i/T} \quad (8)$$

where  $B_i$  is a “barrier” corresponding to the production process.

The combination of these two empirical features powerfully attests to a statistical mechanism of multifragmentation in general, and to liquid-vapor coexistence specifically [12].

Many statistical models have been proposed as an explanation for multifragmentation. It is our intention to identify a model which is as simple as possible, and yet captures the essential features observed in the experiments. The three-dimensional Ising model satisfies both the criteria of simplicity in its Hamiltonian and lends itself to a thermal treatment with nontrivial results [21].

We will show that this model contains both the features of reducibility and thermal scaling observed in nuclear multifragmentation. In showing the features of thermal scaling we will demonstrate that for temperatures below the critical temperature, the slopes of the Arrhenius plots associated with the individual masses of the fragments, or the “barriers”, portray a dependence on the fragment mass ( $A$ ) of the form  $B \propto A^\sigma$ , where  $\sigma$  is a critical exponent which relates the mass to the cluster surface. In addition, the individual Arrhenius plots for each fragment mass can be absorbed into a single scaling function identical to that of Fisher’s droplet model [13, 14, 15, 16, 17], which defines the liquid-vapor coexistence line up to the critical temperature.

The Hamiltonian of the Ising model has two terms: the interaction between nearest neighbor ( $n.n.$ ) spins in a fixed lattice and the interaction between the fixed spins

and an external applied field  $H_{ext}$ :

$$H = -J \sum_{i,j=\{n.n.\}} s_i s_j - H_{ext} \sum_i s_i \quad (9)$$

where  $J$  is the strength of the spin-spin interaction. In the absence of an external magnetic field, the system exhibits a first-order phase transition for temperatures up to the critical point at which it exhibits a continuous phase transition. The critical temperature for the three-dimensional Ising model has not been determined analytically; however, Monte Carlo techniques have yielded a value of  $T_c = 4.513 J/k_b$  [2].

In the present study, Monte Carlo techniques are used to determine equilibrium cluster distributions in a canonical ensemble as a function of temperature for a simple cubic lattice. Since we are interested in studying liquid-vapor coexistence, all calculations are performed at zero external field ( $H_{ext} = 0$ ). The lattice contains  $50^3$  spins, and periodic boundary conditions are used to minimize finite size effects. The Swendsen-Wang algorithm [4] was used to determine the equilibrium spin configurations of the lattice for given temperatures, and physical clusters were identified using the Coniglio-Klein [1] prescription.

We now proceed to analyze the Monte Carlo results in the same way as has been done with nuclear multifragmentation data [9, 10, 11]. We shall consider first whether the multiplicity distributions for individual fragments manifest Poissonian reducibility. Fig. 2 shows the multiplicity distributions for a sample of fragment sizes and temperatures. The solid lines represent Poisson distributions calculated from the corresponding mean multiplicities. The distributions are indeed remarkably close to Poissonian not only for the cases shown, but for all masses and all temperatures below, at and above  $T_c$ . Therefore Poissonian reducibility is empirically verified.

This signifies that the probability of finding  $m$  clusters of size  $A$  depends only on the probability of finding one cluster of that size and is nearly independent of the probability of finding clusters of any other size. This feature is also observed in percolation models, Fisher’s droplet model and nuclear fragmentation [12].

If the fragment distributions exhibit thermal scaling, the distributions must be of the form given in Eq. (8). Thus in an Arrhenius plot (a semi-log graph of the number of clusters of size  $A$  ( $n_A$ ) vs.  $1/T$ ), the distributions should be linear.

As shown in Fig. 2, this is indeed the case over a wide range of temperatures ( $0 < T < T_c$ ) and fragment sizes. While we have shown distributions for clusters up to size  $A = 100$ , the trend continues for larger clusters, but with poorer statistics. This linearity extends over more than four orders of magnitude. It rigorously confirms the form of Eq. (8) and signifies the independent thermal formation of fragments controlled by a size-dependent “bar-

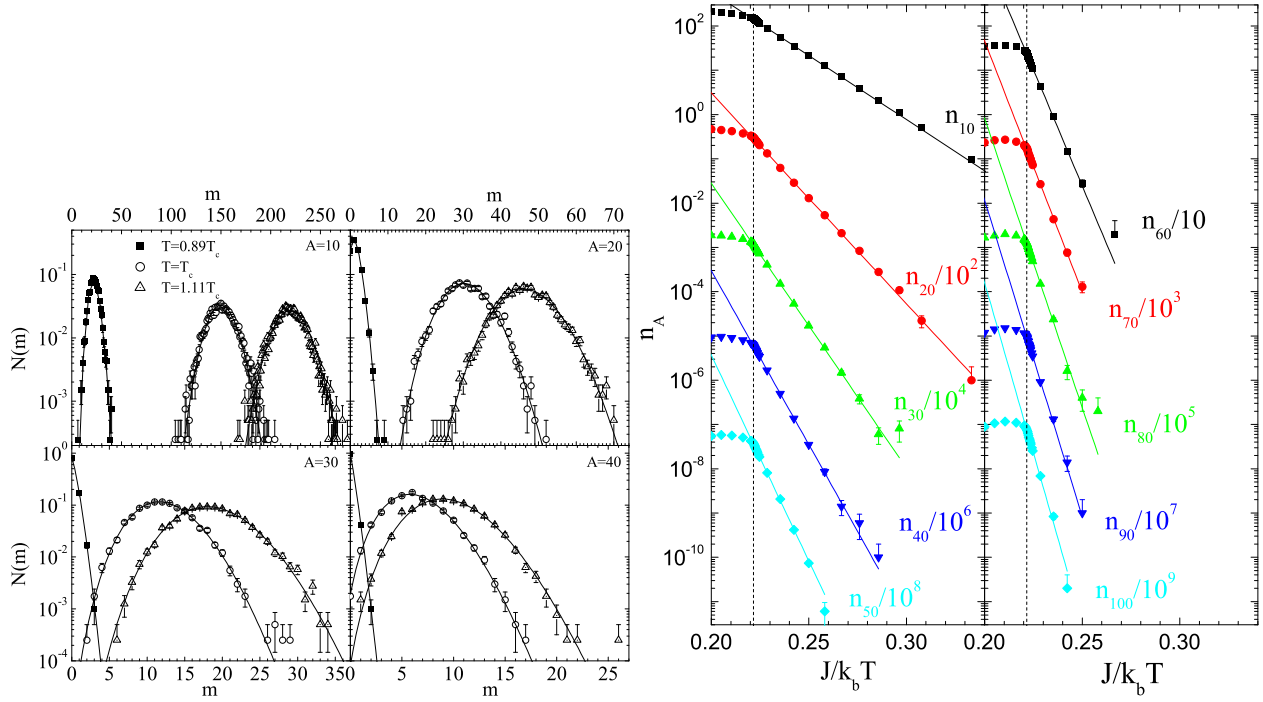


**FIGURE 2.** Left: The probability distributions for obtaining  $m$  fragments of size  $A$  at the three temperatures indicated. The solid lines are Poisson distributions with means given by the Monte Carlo data. Right: Arrhenius plots of the cluster distributions. A statistical error bar is shown when it exceeds the size of the data point. The lines are fits of the form given in Eq. (8). The critical temperature is indicated by the dashed line.

rier”. This feature has been amply verified in nuclear multifragmentation [9, 12, 17]. By fitting the linear regions of the fragment distributions below the critical temperature, the “barriers” can be extracted. The “barriers” for each cluster size are shown in Fig. 3.

These “barriers” find their origin in the number of broken bonds associated with a cluster which should be proportional to the surface area of the cluster itself. Therefore they should be well described by a power-law:

$$B(A) = c_0 A^\sigma. \quad (10)$$

with  $\sigma \simeq 2/3$ . The fit of the extracted “barriers” is  $B = (12.77 \pm 0.04) J A^{(0.723 \pm 0.008)}$  and is remarkably good (see Fig. 3). The error bars are statistical. Estimates of the errors associated with different analysis procedures (described below) increase the errors in  $\sigma$  and  $c_0/J$  to  $\pm 0.026$  and  $\pm 1.2$  respectively.

The value for  $\sigma$  determined from the “barriers” is close to  $2/3$ , the value one would expect for spherical clusters of closely packed spherical objects [3]. This picture leads naturally to the interpretation of  $c_0$  as a surface energy coefficient.

The features of reducibility and thermal scaling discussed above can be found united in Fisher’s formula for the cluster abundance in a vapor as a function of cluster

size and temperature. The formula is

$$n_A(T) = q_0 A^{-\tau} \exp\left(\frac{A\Delta\mu}{T}\right) \exp\left(\frac{c_0 A^\sigma}{T_c}\right) \exp\left(-\frac{c_0 A^\sigma}{T}\right) \quad (11)$$

where  $q_0$  is a normalization constant,  $\tau$  is a topological critical exponent,  $\Delta\mu$  is the difference in chemical potential of the system and the liquid and  $c_0$  is the surface energy coefficient at zero temperature. The formula is valid for temperatures up to the critical point, at which point the surface energy of a cluster ( $c_0 A^\sigma (1 - T/T_c)$ ) vanishes. It contains the thermal scaling up to  $T_c$  and the dependence of the “barrier” on the cluster mass through the critical exponent  $\sigma$  [13, 14, 15, 16]. One can see that the cluster surface energy coefficient ( $c_0$ ) is also found directly in Fisher’s droplet model. It is interesting to explore further the applicability of this formula to the Ising model.

In addition to the linear behavior of the Arrhenius plots below the critical temperature, the Fisher droplet model also predicts that the cluster size distribution at the critical temperature must follow a power law

$$n_A(T_c) = q_0 A^{-\tau}. \quad (12)$$

The best power law fit of the fragment abundances is shown in the lower panel of Fig. 3. The critical temperature was found to be  $k_b T_c/J = 4.515 \pm 0.011$  with a best

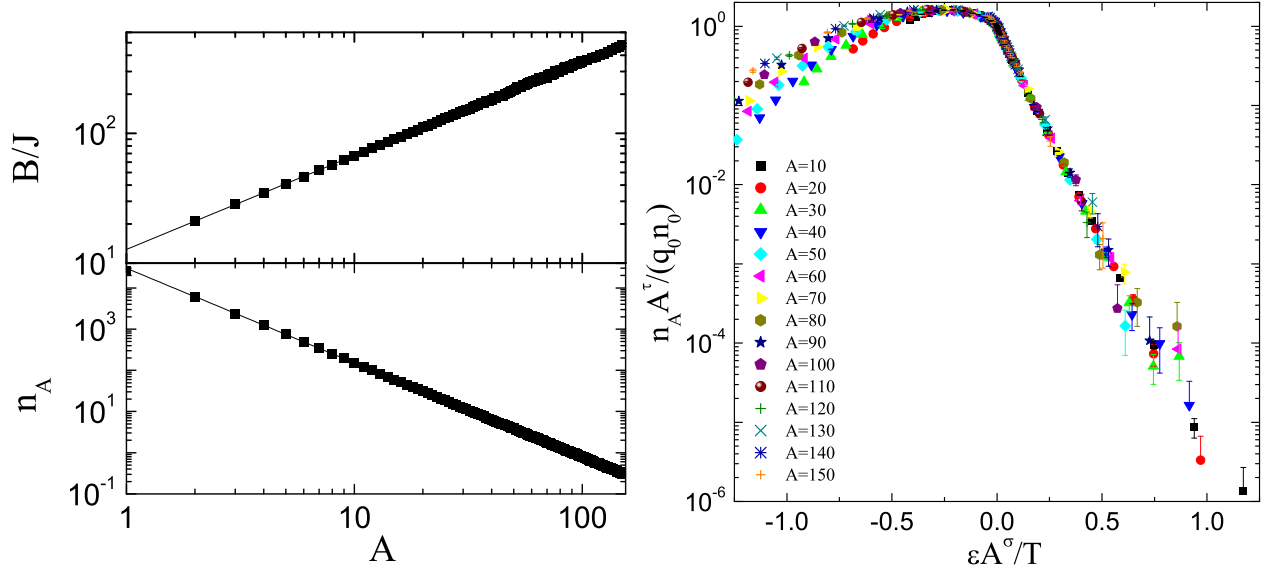


**FIGURE 3.** Left: The upper panel shows the extracted “barriers” from the fits to the cluster distributions. The line is a fit of the form given in Eq. (10). The lower panel shows the power law behavior of the cluster distribution at  $k_b T/J = 4.515$ . The line is a fit of the form given in Eq. (12). In both panels, error bars are smaller than the data point. Right: Scaling behavior of cluster distributions.

fit of the form  $n_A(T_c) = (30,000 \pm 5,000)A^{(-2.30 \pm 0.08)}$ . This value of the critical temperature is consistent with the value determined for infinite systems ( $4.513J/k_B$ ).

For the present calculations with  $H_{ext} = 0$  and an unconstrained magnetization, the system exists on the coexistence curve for  $T < T_c$ . Thus, the chemical potentials of the liquid and gas phases are equal ( $\Delta\mu = 0$ ), and Eq. (11) can be rewritten as:

$$n_A(T)A^\tau/q_0 = \exp(-c_0 A^\sigma \epsilon/T) \quad (13)$$

with  $\epsilon = (T_c - T)/T_c$ . Therefore, a graph of the scaled cluster distributions ( $n_A(T)A^\tau/q_0$ ) as a function of  $\epsilon A^\sigma/T$  should collapse the distributions of all cluster sizes onto a single curve. This scaling behavior can clearly be seen in Fig. 3. This nearly perfect collapse below the critical temperature extends over six orders of magnitude for a broad range of cluster sizes and it is very linear. Thus the clustering in the three-dimensional Ising model can be described by Fisher’s droplet model.

The Ising clusters constructed here can be properly thought of as “vapor” in equilibrium with the “liquid” percolating cluster. Coexistence of the two phases is determined by the observation that the empirical scaling implies  $\Delta\mu = 0$ . The fact that both the three-dimensional Ising model and the experimental nuclear multifragmentation data obey the same scaling predicted by Fisher’s droplet model indicates that nuclear multifragmentation can indeed be identified as the clustering (non-ideality) in a nuclear vapor in equilibrium with the nuclear liquid [12, 17].

In conclusion, we have shown that the clusterization in the Ising model, like nuclear multifragmentation, portrays reducibility and thermal scaling. In addition, the Arrhenius plots allow for the extraction of “barriers” which are found to have a dependence of  $B = c_0 A^\sigma$ , where  $\sigma$  is a critical exponent. The “barrier” coefficient from the Arrhenius plots is equivalent to the surface energy coefficient of the clusters in Fisher’s model. Thus we have found a new method for determining both the critical exponent  $\sigma$  and the surface energy of the 3-D Ising model clusters directly from the cluster distributions. The reducibility and thermal scaling features in the Ising model can be incorporated into a Fisher-like scaling with  $\Delta\mu = 0$ , which is obeyed rigorously over the explored temperature range below the critical temperature. Thus the observed clusters can be interpreted as a manifestation of the non-ideality of a vapor in equilibrium with a liquid. Finally, nuclear multifragmentation, which is seen to share all the scaling observed here, should be similarly interpreted as the clusterization of a nuclear vapor in equilibrium with its liquid.

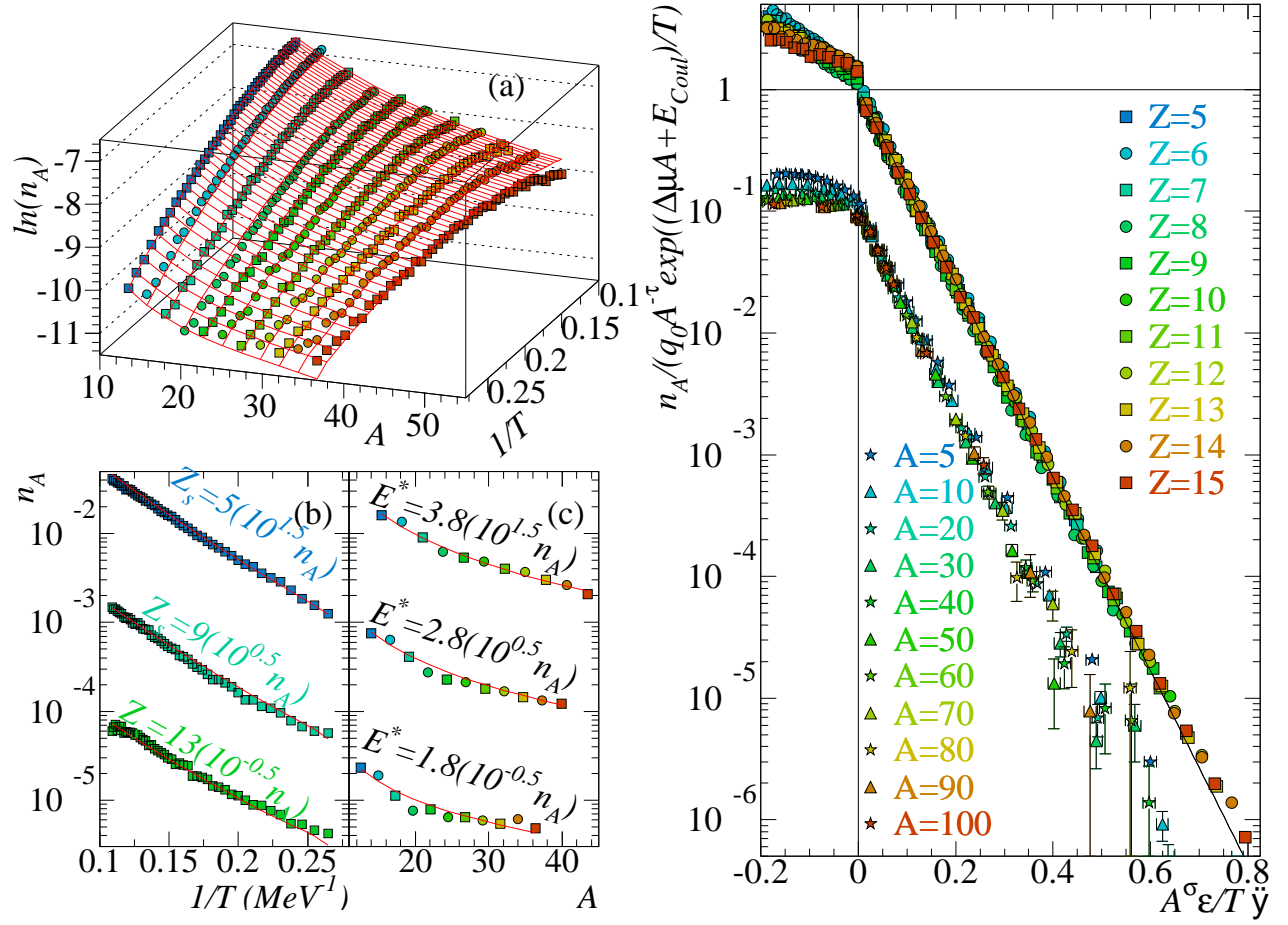


**FIGURE 4.** Left: (a) The ISiS fragment yield surface: natural log of the fragment yield vs. fragment mass and inverse temperature. (b) Arrhenius plots for representative charges. (c) Fragment mass yields for various values of  $E^*$ . Solid curves are from a fit to Fisher's model. Error bars are smaller than the size of the points. Right: The scaled yield distribution versus the scaled temperature for the ISiS data (upper) and  $d = 3$  Ising model calculation (lower). For the Ising model, the quantity  $(n_A/q_0 A^{-\tau})/10$  is plotted against the quantity  $A^\sigma \epsilon/1.435T$ . Data for  $T > T_c$  is scaled only as  $n_A/q_0 A^{-\tau}$ .

# EXPERIMENTAL PROPERTIES OF THE NUCLEAR VAPOR AND THE PHASE DIAGRAM

## The ISiS data sets

Recently, multifragmentation data from the Indiana Silicon Sphere (ISiS) Collaboration was shown to exhibit both reducibility and thermal scaling [22, 23]; thus it may be interesting to determine whether the Fisher model describes the ISiS data as well. In order to find if this is the case, the ISiS charge yields from AGS experiment E900a of 8 GeV/c  $\pi + \text{Au}$  fragmentation data (see Fig. 4a) were fit to the following modified form of Eq. (11) which incorporates, in an approximate manner, the Coulomb energy release when a particle moves from the liquid to the vapor:

$$n_A = q_0 A^{-\tau} \exp \left( \frac{A\Delta\mu + E_{Coul}}{T} - \frac{c_0 \epsilon A^\sigma}{T} \right), \quad (14)$$

where  $E_{Coul}$  is given by:

$$E_{Coul} = \frac{e^2}{4\pi\epsilon_0} \frac{(Z_0 - Z)Z}{r_0 \left( (A_0 - A)^{1/3} + A^{1/3} \right)} (1 - e^{-x\epsilon}). \quad (15)$$

Here  $Z_0$  is the charge of the fragmenting system and  $r_0 = 1.2$  fm. This energy vanishes as  $x\epsilon$  at the critical point where no distinction exists between liquid and vapor. The mass of a fragment prior to secondary decay  $A$  was estimated by multiplying the measured fragment charge  $Z$  by an  $A/Z$  ratio of 2 and by a factor of  $(1 + (E^*/B_f))$  where  $E^*$  is the reconstructed excitation energy of the event and  $B_f$  is the binding energy of the fragment. The temperature  $T$  was determined by assuming a degenerate Fermi gas, thus  $T = \sqrt{E^*/a}$  and  $a = A_0/\alpha$ ;  $\alpha = 8(1 + E^*/B_0)$  [24] with  $B_0$  as the binding energy of the fragmenting system. This accommodates the empirically observed change in  $\alpha$  with excitation energy [25].

Over 500 data points for  $1.5 \leq E^* \leq 6.0$  MeV/nucleon and  $5 \leq Z \leq 15$  were simultaneously fit to Eq. (14) with the parameters of the modified Fisher model ( $\Delta\mu$ ,  $x$ ,  $\tau$ ,  $\sigma$ ,  $c_0$  and  $T_c$ ) allowed to vary to minimize chi-squared (see Fig. 4a). Fragments with  $Z < 5$  were not considered in the fit because: (1) Fisher's model expresses the mass/energy of a fragment in terms of bulk and surface energies and this approximation is known to fail for the lightest of nuclei where structure details (shell effects) dominate, and (2) for the lightest fragments equilibrium and non-equilibrium production cannot always be differentiated. Fragments with  $Z > 15$  were not elementally resolved [26], and were also excluded.

The behavior of the data for the  $(n_A, A, T)$  surface is reproduced over a wide range in  $E^*$  and  $Z$  as shown in

both Arrhenius plots (Fig. 4b) and fragment yield distributions (Fig. 4c). The results of scaling the data according to Eq. (14) are shown in Fig. 4. The fragment mass yield distribution is scaled by the Fisher's power law pre-factor, the bulk term and the Coulomb energy:  $n_A/q_0 A^{-\tau} \exp(\Delta\mu A + E_{Coul}/T)$ . This quantity is plotted against the temperature scaled by Fisher's parameterization of the surface energy:  $A^\sigma \epsilon/T$ . The scaled data collapse to a single line over six orders of magnitude, precisely the behavior predicted by Fisher's model. This line is the liquid-vapor coexistence line, as shown below, and provides direct evidence for the liquid to vapor phase transition in excited nuclei. It may be worth noticing that Fig. 4 represents the first extensive test ever for any physical system of Fisher's formula (Eq. (11)).

The value of  $\tau = 2.18 \pm 0.14$  is in the range predicted by Fisher's model and  $\sigma = 0.54 \pm 0.01$  is close to the value expected for a three dimensional system,  $\sim 2/3$ . The  $\Delta\mu = 0.06 \pm 0.03$ , may indicate that the system is a slightly super-saturated vapor. The value of  $x$  is  $1.00 \pm 0.06$ . The value of  $c_0 = 18.3 \pm 0.5$  MeV is close to the value of the surface energy coefficient of the liquid-drop model: 16.8 MeV. The values of the critical exponents determined here are in agreement with those determined previously from other multifragmentation data [19, 20] and the value of the excitation energy at the critical point  $E_c^* = 3.8 \pm 0.3$  MeV/nucleon is in the neighborhood of the value observed in the EOS analysis ( $E_c^* \approx 4.75$  MeV/nucleon) [12, 20, 28]. The two experiments use a different method to distinguish *particles* resulting from the initial projectile-target collision from *fragments* formed afterwards; this difference leads to  $^{EOS}E^* \approx 1.2^{ISiS}E^*$  [27]. The value of  $^{EOS}E_c^*$  corresponds to the steepest decrease in the mass of the largest fragment and to the maximum value of its variance in the EOS data [20, 28]. The extracted critical temperature  $T_c = 6.7 \pm 0.2$  MeV is comparable to theoretical estimates for small nuclear systems [30, 31, 32, 33].

Using the values of the parameters determined above for the ISiS experiment and Eq. (14), the coexistence curve observed in the scaled fragment yields in Fig. 4 can be cast into a more familiar form. Fisher's model assumes that the non-ideal vapor can be approximated by an ideal gas of clusters. Accordingly, the quantity  $n_A$  is proportional to the partial pressure of a fragment of mass  $A$  and the total pressure due to all of the fragments is the sum of their partial pressures:  $p/T = \sum n_A$ . In the actual experiment, this pressure is virtual, it is the pressure the vapor would have to provide the back flow needed to keep the source at equilibrium. The reduced pressure is given by:

$$\frac{p}{p_c} = \frac{T \sum n_A(T)}{T_c \sum n_A(T_c)}. \quad (16)$$

The coexistence line for finite neutral nuclear matter is



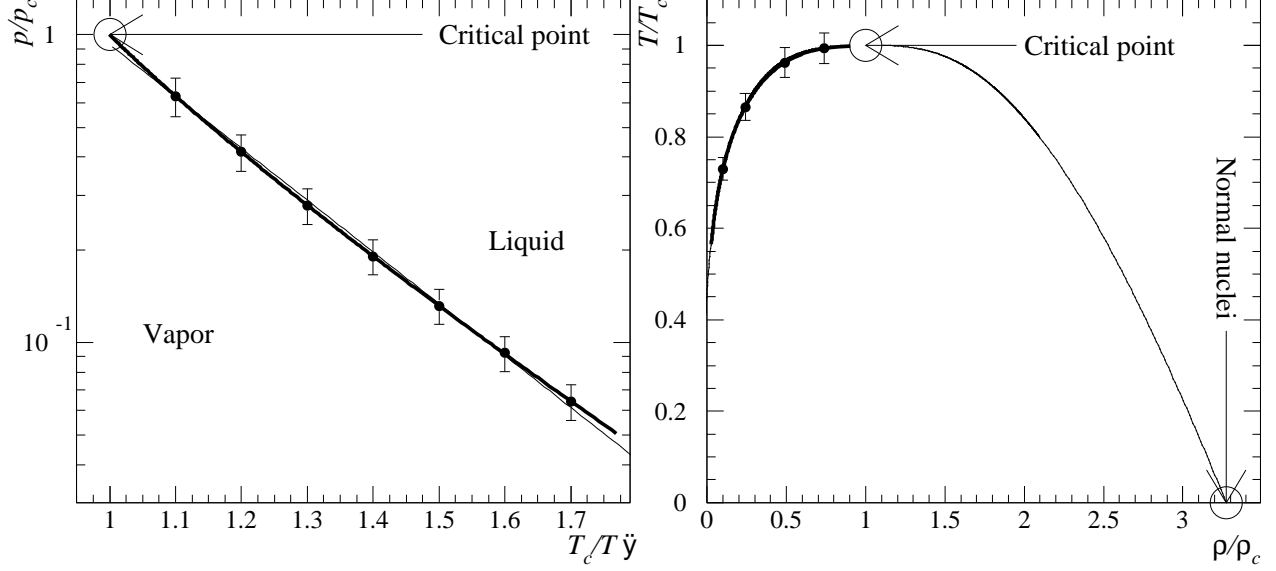


**FIGURE 5.** Left: The reduced pressure-temperature phase diagram: the thick line shows the calculated coexistence line, the points show selected calculated errors and the thin line shows a fit to the Clausius-Clapeyron equation. Right: The reduced density-temperature phase diagram: the thick line shows the calculated low density branch of the coexistence curve, the points show selected calculated errors and the thin lines show a fit to and reflection of Guggenheim's equation.

then obtained by using the  $n_A(T, \Delta\mu = 0, E_{Coul} = 0)$  from Eq. (14) in Eq. (16). This is shown in Fig. 5. Recalling the Clausius-Clapeyron equation:  $dp/dT = \Delta H/T\Delta V$  one obtains:  $p/p_c = \exp(\Delta H/T_c(1 - T_c/T))$  which describes several fluids up to  $T_c$  [36]. Fitting the coexistence line and using the above value of  $T_c$  gives  $\Delta H = 26 \pm 1$  MeV, the enthalpy of evaporation of a cluster from the liquid. This value, after a correction  $pV = T$ , gives a value for  $\Delta E \approx 22$  MeV. Since the gas described by Fisher's model is non-ideal, the average cluster is greater in size than a monomer. The average size of a fragment in the region of the  $p$ - $T$  coexistence line obtained from Eq. (14) and the experimentally determined parameters is 1.5. Thus the  $\Delta E$ /nucleon becomes  $\approx 15$  MeV, remarkably close to the nuclear bulk energy coefficient.

The system's density can be found from  $\rho = \sum A n_A$ , and the reduced density from

$$\frac{\rho}{\rho_c} = \frac{\sum A n_A(T)}{\sum A n_A(T_c)}. \quad (17)$$

With  $\Delta\mu$  and  $E_{Coul}$  set to 0 in Eq. (14), Eq. (17) yields the low density branch of the coexistence curve of finite neutral nuclear matter, shown in Fig. 5. Following Guggenheim it is possible to determine the high density branch as well: empirically, the  $\rho/\rho_c$ - $T/T_c$  coexistence curves of several fluids can be fit with the function [37]:

$$\frac{\rho_{l,v}}{\rho_c} = 1 + b_1\left(1 - \frac{T}{T_c}\right) \pm b_2\left(1 - \frac{T}{T_c}\right)^{1/3} \quad (18)$$

where the parameter  $b_2$  is positive (negative) for the liquid  $\rho_l$  (vapor  $\rho_v$ ) branch. It was later recognized that

the power of  $1/3$  was the critical exponent  $\beta$ . Using Fisher's model,  $\beta$  can be determined from  $\tau$  and  $\sigma$ :  $\beta = (\tau - 2)/\sigma$  [13, 14, 15, 16]. For this work  $\beta = 0.33 \pm 0.25$ . Using this value of  $\beta$  and fitting the coexistence curve from the ISiS E900a data with Eq. (18) one obtains an estimate of the full  $\rho_v$  branch of the coexistence curve and changing the sign of  $b_2$  gives the full  $\rho_l$  branch of the coexistence curve of finite neutral nuclear matter. If normal nuclei exist at the  $T = 0$  point of the coexistence curve and the parameterization of the coexistence curve in Eq. (18) is used, then the critical density is found to be  $\rho_c \sim 0.3\rho_0$ .

The critical compressibility factor  $C_c^F = p_c/T_c\rho_c$  is found to be  $0.25 \pm 0.06$ , in agreement with the values for several fluids [38]. Using  $T_c$  and  $\rho_c$  from above in combination with  $C_c^F$  gives a critical pressure of  $p_c \sim 0.07$  MeV / fm<sup>3</sup>.

## The EOS data sets

The EOS Collaboration has collected data for the reverse kinematics reactions 1.0 AGeV Au+C, 1.0 AGeV La+C and 1.0 AGeV Kr+C [28, 29]. There were  $\sim 25,000$ ,  $\sim 22,000$  and  $\sim 36,000$  fully reconstructed events recorded for the Au+C, La+C and Kr+C reactions, respectively. The term "fully reconstructed" means that the total measured charge in each event was within three units of the charge of the projectile.

The location of the critical point, in terms of excitation energy, was determined from an examination of measured fluctuations. This was not possible with the ISiS data set because there was no direct measure of the largest fragment in each event and the events were not fully reconstructed. At the critical point the fluctuations are maximal. However, while the maximum in the fluctuations will occur at the critical point, the presence of a peak in the fluctuations is a necessary, but not sufficient, condition for a existence of a phase transition [20]. Table 1 lists the results. For this analysis the values determined for the excitation energy at the critical point for the Au+C reaction are in proximity of other values observed in previous EOS analyses ( $E_c^* \approx 4.75$  MeV/nucleon) [20, 12, 28, 29]. Estimates of the critical temperature  $T_c$  are made by using the values of  $E_c^*$  via the degenerate Fermi gas relation as above and led to values, shown in Table 1, that are comparable to theoretical estimates for small nuclear systems [30, 31, 32, 33].

Figure 6 shows the fragment mass yield distribution scaled by the power law pre-factor, the chemical potential and Coulomb terms:  $n_A/q_0 A^{-\tau} \exp(\Delta\mu A + E_{Coul}/T)$  plotted against the inverse temperature scaled by Fisher's parameterization of the surface energy:  $A^\sigma \epsilon/T$ . Now, the scaled data for all three systems collapse onto a single line over several orders of magnitude as predicted by Fisher's droplet formalism [13]. This collapse provides direct evidence for a liquid to vapor phase transition in excited nuclei. Furthermore, the fact that the data from each system show a common scaling illustrates the common nature of the underlying phenomenon.

The values of  $\tau = 2.2 \pm 0.1$ ,  $\sigma = 0.71 \pm 0.02$  and  $c_0 = 14.0 \pm 1.0$  MeV determined in this analysis are in agreement with those determined for the ISiS gold multifragmentation data sets [17] and are in agreement with values previously determined for the EOS Au+C data set [18, 34, 35, 20, 12]. The value of the surface energy coefficient  $c_0$  is close to the value of the surface energy coefficient of the liquid-drop model which is 16.8 MeV.

The values of  $\Delta\mu$  reported in Table 2 should be compared to the values returned when the EOS fragment yields were fit to (Eq. 11):  $\langle\Delta\mu\rangle \approx 3.0$  A MeV for all EOS reactions. The reduction in the magnitude of the  $\Delta\mu$  values is about a factor of six and is due to the modification of Eq. (11) to account for the Coulomb energy, i.e. Eq. (14). The remaining small positive  $\Delta\mu$  values of the systems may indicate that those systems are slightly super-saturated, or more probably they may reflect some other energy costs not taken into account (e.g. the symmetry energy or pairing), or they may reflect that the approximation for the cost in Coulomb energy to form a fragment given in Eq. (15) is not completely adequate (for instance Eq. (15) assumes a spherical geometry which may or may not be the case) or the may merely

reflect noise in the data.

The values of  $x$  for each system may indicate more (Au and La) or less (Kr) Coulomb energy present in the system. They may also reflect the symmetry of the collision which may affect the geometry of the remnant, e.g. a very asymmetric collisions like Au+C may leave a nearly spherical remnant, while a more symmetric collision like Kr+C may result in a less spherical fragmenting system.

The values of  $y$  returned indicate that the fragments have the same mass to charge ratio as the excited remnant.

The difference in values of  $\Delta\mu$ ,  $x$  and  $y$  determined in the analysis of the three EOS data sets and those determined in the analysis of the ISiS 8.0 GeV/c  $\pi$  on gold multifragmentation set [17] is also an open question. The differences in  $E_c^*$  and  $T_c$  are due to the differences in reconstructed excitation energy scales [27]. This difference carries over to all energy related quantities, e.g.  $c_0$ .

The  $p$ - $T$  coexistence curve can be determined from this analysis. As seen above, Fisher's theory assumes that the non-ideal fluid can be approximated by an ideal gas of droplets. Accordingly, the quantity  $n_A$  is proportional to the partial pressure of a fragment of mass  $A$  and the total pressure due to all of the fragments is the sum of their partial pressures. The reduced pressure is then given by Eq. (16). The coexistence curve for finite neutral nuclear matter is obtained by substituting the  $n_A(T, \Delta\mu = 0, E_{Coul} = 0)$  from Eq. (14) in the numerator of Eq. (16) and  $n_A(T_c, \Delta\mu = 0, E_{Coul} = 0)$  in the denominator. This allows one to transform the information in Fig. 6 into the familiar phase diagram in Fig. 7. The data points shown give the values of  $p/p_c$  and  $T_c/T$  calculated via Eq. (16) for the bins in  $E^*$  up to and including the critical point.

Figure 7 gives an estimate of the coexistence line of finite nuclear matter and from this it is possible to make an estimate of the bulk binding energy of nuclear matter and the  $\Delta E/A \approx 14$  A MeV, close to the nuclear bulk energy coefficient of 15.5 MeV.

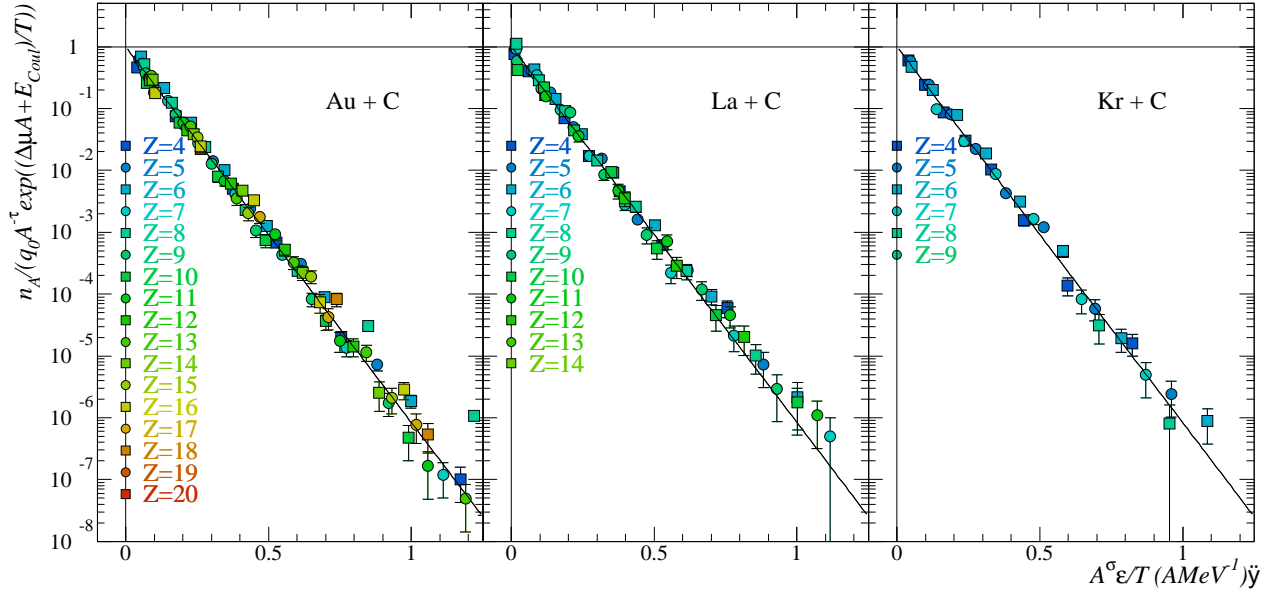
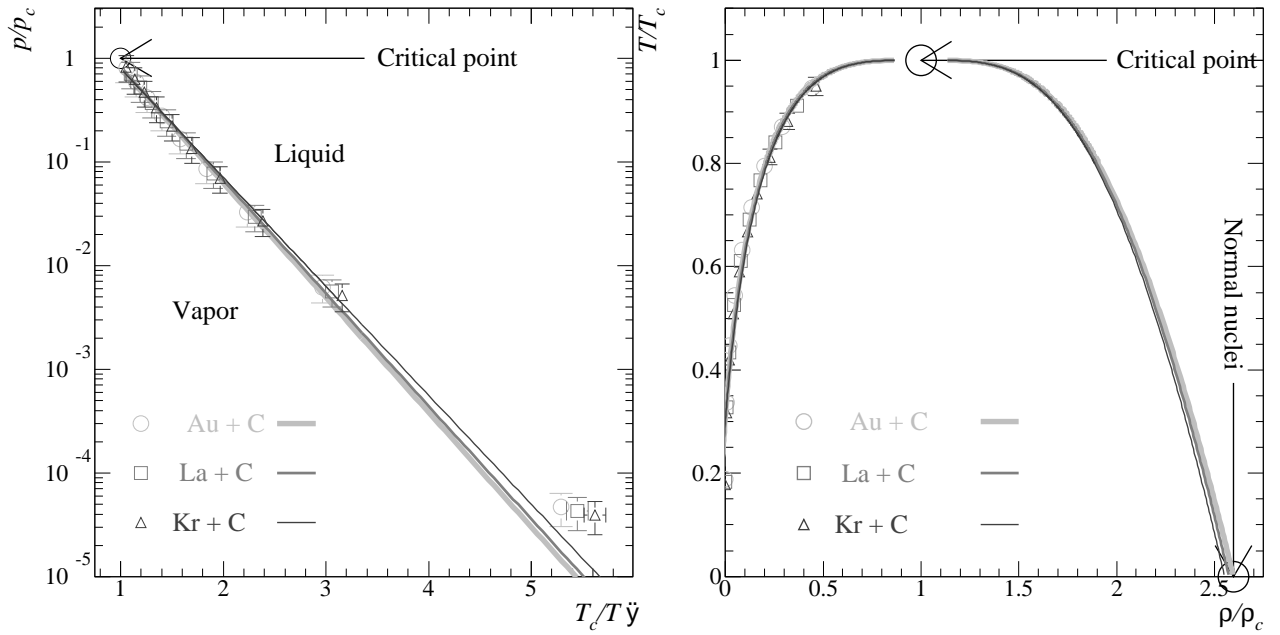
The reduced density is given by Eq. (17). With  $\Delta\mu$  and  $E_{Coul}$  set to 0 in the numerator of Eq. (14) and  $\Delta\mu$  and  $E_{Coul}$  set to 0 with  $T$  set to  $T_c$  in the denominator, Eq. (17) gives the low density branch of the coexistence curve of finite nuclear matter, shown in Fig. 7.

Following Guggenheim's work with simple fluids it is possible to determine the high density branch as well via Eq. (18). For the EOS data  $\beta = 0.3 \pm 0.1$ . Using this value of  $\beta$  and fitting the coexistence curve from the EOS data sets with Eq. (18) one obtains estimates of the  $\rho_v$  branch of the coexistence curve and changing the sign of  $b_2$  gives the  $\rho_l$  branch, thus yielding the full  $T$ - $\rho$  coexistence curve of finite nuclear matter.

From Fig. 7 it is possible to make an estimate of the density at the critical point  $\rho_c$ . Assuming that normal

**TABLE 1.** Critical points of excited nuclei

System	$E_c^*$ (AMeV)	$T_c$ (MeV)	$\rho_c$ ( $\rho_0$ )	$p_c$ (MeV/fm <sup>3</sup> )
Au + C	$4.6 \pm 0.2$	$7.6 \pm 0.2$	$0.39 \pm 0.01$	$0.11 \pm 0.04$
La + C	$4.9 \pm 0.2$	$7.8 \pm 0.2$	$0.39 \pm 0.01$	$0.12 \pm 0.04$
Kr + C	$5.1 \pm 0.2$	$8.1 \pm 0.2$	$0.39 \pm 0.01$	$0.12 \pm 0.04$

**FIGURE 6.** The scaled yield distribution versus the scaled temperature for the gold, lanthanum and krypton systems. The solid line has a slope of  $c_0$ .**FIGURE 7.** EOS data results. Left: The reduced pressure-temperature phase diagram: the points show calculations performed at the excitation energies below the critical point and the lines show fits to the Clausius-Clapeyron equation. Right: The points are calculations performed at the excitation energies below the critical point and the lines are a fit to and reflection of Guggenheim's equation.

**TABLE 2.** Uncommon fit parameters

System	$\Delta\mu$ (AMeV)	$x$	$y$
Au + C	$0.38 \pm 0.02$	$1.1 \pm 0.2$	$0.5 \pm 0.1$
La + C	$0.47 \pm 0.03$	$1.2 \pm 0.1$	$0.3 \pm 0.2$
Kr + C	$0.58 \pm 0.08$	$4.0 \pm 1.0$	$0.8 \pm 0.2$

nuclei exist at the  $T = 0$  point of the  $\rho_l$  branch of the coexistence curve, then using the parameterization of the coexistence curve in Eq. (18) gives  $\rho_c \sim \rho_0/3$ . See Table 1 for precise values.

The critical compressibility factor  $C_c^F = p_c/T_c\rho_c$  can also be determined in a straightforward manner from [38] via  $C_c^F = p_c/T_c\rho_c$  and Table 3 shows the results for the EOS data sets which are in agreement with the values for several fluids [15] and that of the ISiS data [17].

Finally, a measure of the pressure at the critical point  $p_c$  can be made by using  $T_c$  and  $\rho_c$  from above in combination with  $C_c^F$ . The results are shown in Table 1. This last calculation gives a complete experimental measure of the location of the critical point of finite nuclear matter ( $p_c, T_c, \rho_c$ ) and is in agreement with the ISiS results and in rough agreement with theoretical calculations [30, 33].

## FINITE SIZE EFFECTS AND THE EXTRAPOLATION TO INFINITE NUCLEAR MATTER

The coexistence line and phase diagram obtained above refer to well specified nuclei, which are finite systems. Our goal, in this section, is to extrapolate these results to infinite nuclear matter.

Finite size effects are paramount in nuclei. For instance, the binding energy per nucleon decreases from the  $\sim 15.5$  AMeV calculated for nuclear matter to about 8 AMeV for typical nuclei. This lowering of the binding energy is understood as due to the surface (and Coulomb) energy.

We can expect that such a drastic reduction affects the critical temperature as well. The Ising model can be used again as a simple testing ground. Like in nuclei, we have a volume energy: if a finite system is considered (no periodic boundary conditions) a surface is generated with the attendant surface energy. This allows us to write a “liquid drop” formula for the Ising model:

$$E = a_V A + a_S A^{2/3}. \quad (19)$$

In most fluids for which a liquid drop expansion is applicable the volume coefficient  $a_V$  is approximately equal and opposite to the surface coefficient  $a_S$ :  $a_V \approx -a_S$ . This is true for nuclei and it is expected for the Ising model.

We now determine the critical temperature for various sizes (lattices) and check its dependence on the lattice size. Figure 8 shows a remarkable decrease of  $T_c$  with decreasing lattice size which we are now trying to understand. The infinite Ising model contains a single parameter that determines the energy scale and thus the binding energy per site. We now naively guess that, for a finite system also all the quantities are expressed in energy scale with the binding energy per site, but corrected for the surface energy. We can write

$$\frac{T_c^{A_0}}{T_c^\infty} = \frac{a_V A_0 + a_S A_0^{2/3}}{a_V A_0} = 1 - \frac{1}{A_0^{1/3}} = 1 - \frac{1}{L} \quad (20)$$

where  $A_0$  is the number of sites in the lattice and  $L$  is the linear lattice side. This naive version of the finite size scaling of the critical temperature has been discussed long ago [39] and more sophisticated versions have been theorized [39] and observed such as [40, 5]

$$\frac{T_c^{A_0}}{T_c^\infty} \propto 1 - L^{-1/\nu} \quad (21)$$

where  $\nu$  is the critical exponent describing the divergence of the correlation length near the critical point. For the three-dimensional Ising lattice  $\nu \approx 0.63$ . For the purposes at hand, the naive finite size scaling is sufficient and the sophisticated version produces essentially equivalent results shown in Figure 8.

The result of this exercise is to show that the critical temperature of infinite nuclear matter should be approximately equal to that determined above for finite nuclei time the ratio of the binding energy of infinite nuclear matter to the binding energy of the finite nucleus. In fact, we can do better than that. In each of the three EOS reactions, remnants of different sizes (and thus of different critical temperatures) are characterized. In this way a good range of  $A_0$  values is accessible. Now we can try to fit the entire universe of EOS data as done above, but using the scaling give by Eq. (20).

We do this by performing the Fisher scaling fit as above, but in  $\varepsilon$  in Eq. (14) use  $T_c(A_0)$  from Eq. (20) and  $T_c(\infty)$  left as a fit parameter. The preliminary results are shown in Fig. 9 when this is done for both the EOS and ISiS data sets individually. The fit parameters are almost the same as in the previous analysis and are shown in Table 4. The extracted values for the critical temperature of infinite nuclear matter are  $\sim 13.6$  MeV from the ISiS data and  $\sim 12.9$  MeV from the EOS data. These values agree well with various theoretical estimates of the critical temperature of bulk nuclear matter.

The distribution of  $T_c(A_0)$  is shown in Fig. 10. The value of  $T_c(A_0)$  resembles the nuclear binding energy curve because for a nucleus Eq. (20) becomes

$$\frac{T_c^{A_0}}{T_c^\infty} = \frac{B(A_0, Z_0)}{B(\infty, 0)} \quad (22)$$

**TABLE 3.** Thermodynamic properties of excited nuclei

System	$\Delta H$ (MeV)	$\langle T \rangle$ (MeV)	$\Delta E/A$ (AMeV)	$C_c^F$
Au + C	$19.4 \pm 0.7$	$4.6 \pm 0.6$	$14 \pm 1$	$0.28 \pm 0.09$
La + C	$19.6 \pm 0.7$	$4.9 \pm 0.6$	$14 \pm 1$	$0.28 \pm 0.09$
Kr + C	$19.5 \pm 1.7$	$4.9 \pm 0.6$	$14 \pm 1$	$0.28 \pm 0.09$

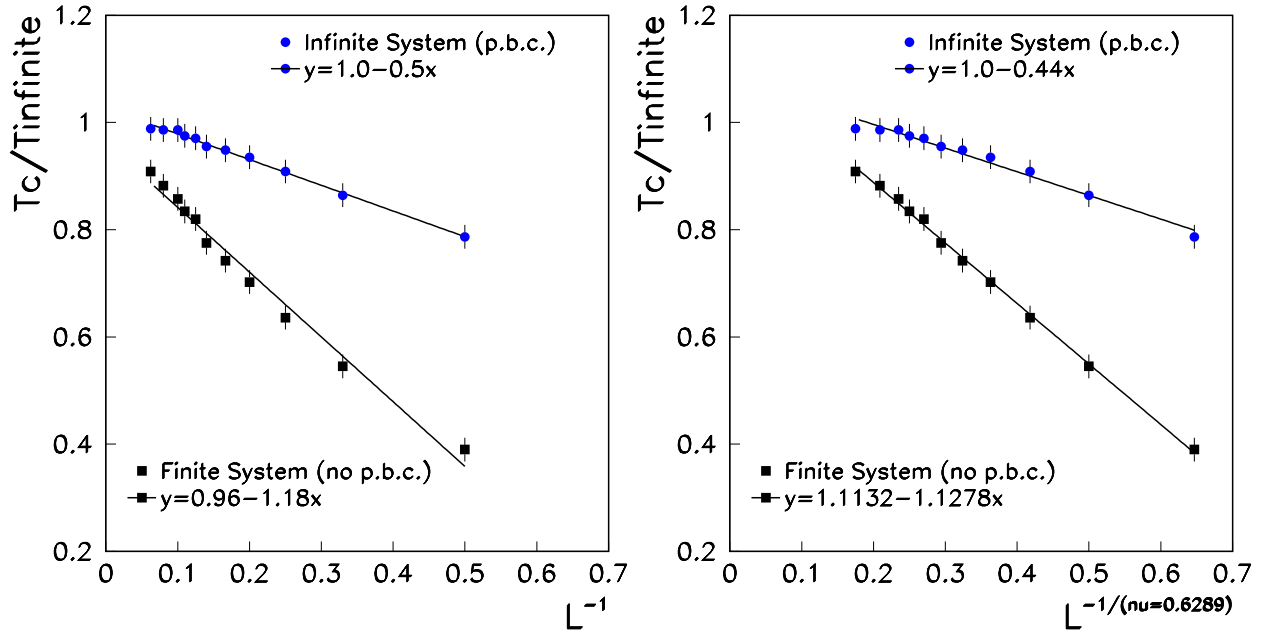


**FIGURE 8.** Finite size scaling of the critical temperature of the three-dimensional Ising model. Left: the naive estimate of finite size scaling. Right: the sophisticated estimate of finite size scaling. The data points and fits on the top of both figures show the results for lattices with periodic boundary conditions (p.b.c.) which more closely represent an infinite system. The datapoints and fits on the bottom of both figures show the results for lattices with open boundary condition (no p.b.c.) and more closely represent the case of finite systems like nuclei.

**TABLE 4.** Uncommon fit parameters

System	$\Delta\mu$ (AMeV)	$x$	$y$	$\sigma$	$\tau$	$c_0$ (MeV)
ISiS $\pi$ + Au	$\sim 0.1$	$\sim 1.1$	1.0 (fixed)	$\sim 0.6$	$\sim 2.2$	$\sim 18.1$
EOS Au + C	$\sim 0.2$	$\sim 1.0$	$\sim 0.7$	$\sim 0.6$	2.2 (fixed)	$\sim 16.6$
EOS La + C	$\sim 0.2$	$\sim 1.2$	$\sim 0.4$	$\sim 0.6$	2.2 (fixed)	$\sim 16.6$
EOS Kr + C	$\sim 0.5$	$\sim 3.0$	$\sim 0.8$	$\sim 0.6$	2.2 (fixed)	$\sim 16.6$

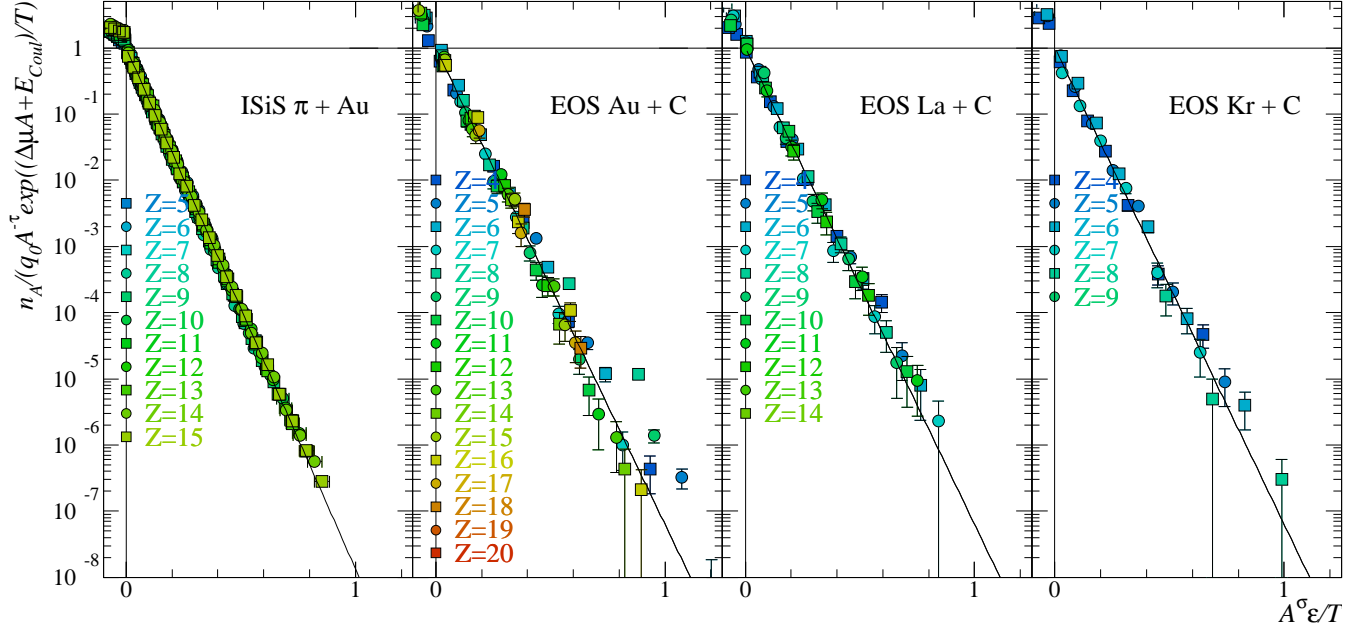


**FIGURE 9.** Fisher scaling and finite size scaling analysis of the ISiS and EOS data sets.

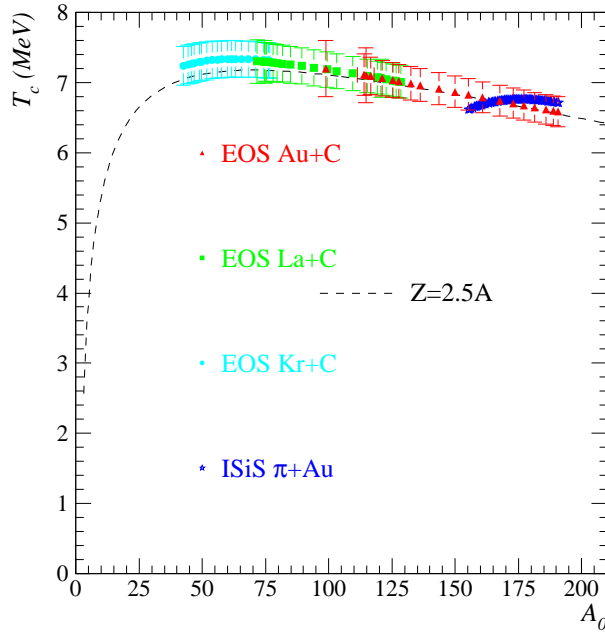


**FIGURE 10.** Variation of the critical temperature with nucleon number for the EOS and ISiS fragmenting remnants.

the ratio of the binding energy of a given nucleus of mass  $A_0$  and charge  $Z_0$  to the bulk binding energy.

## COMPOUND NUCLEUS DECAY AND THE LIQUID TO VAPOR PHASE TRANSITION

The construction of a phase diagram, and in particular of a pressure-temperature diagram for a nuclear system leads us to the inevitable question: What is the meaning of pressure when the nuclear system is facing vacuum? This question has presented itself in many equivalent guises in the literature and in endless discussions. It amounts to asking: a) whether there is a gas phase in equilibrium with a liquid for the reactions in question; and b) whether this gas phase is thermodynamically characterizable.

The answer is no to a) and yes to b). And this is not contradictory. Consider the interface between a liquid and saturated vapor. From the liquid side we can specify with standard theories (e.g. compound nucleus decay rate, the equation for electrons emitted from a hot filament, etc.) the emission flux of particles from the surface. See Fig. 11. From the vapor side, we can write down the return flux into the liquid knowing the temperature, pressure/concentration and composition of the vapor. At equilibrium, by definition, the vapor to liquid flux matches physically and chemically the liquid to vapor flux. Thus, the saturated vapor acts, so to speak, as a mirror reflecting back elastically all the particles emitted by the liquid. This is the only role of the vapor.

If we remove the vapor, the liquid continues emitting particles as if the vapor were still present. Thus, the sat-

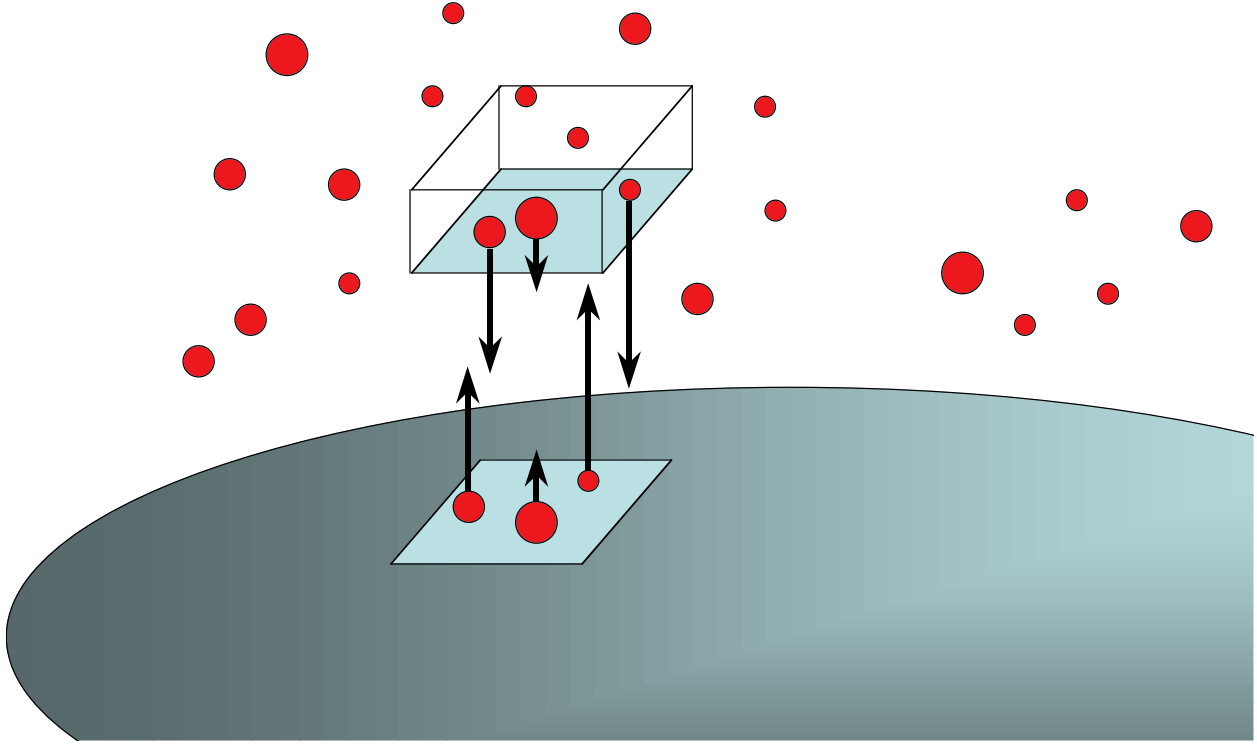


**FIGURE 11.** Emission of nuclear droplets from a compound nucleus.

urated vapor is completely characterized by the flux from the liquid side, even if the vapor itself is not physically there. So it is that we can unequivocally speak of the phase transition for a glass of water (or a nucleus) evaporating in a dry atmosphere or equivalently in vacuum.

In this light, compound nuclear decay becomes suddenly relevant to the liquid to vapor phase transition. In the past, we have studied the evaporation of complex fragments from well characterized compound nuclei [41]. It should be possible to cast these results in terms of Fisher's scaling. This is done in Fig. 12 for the reaction of Ni+C. As in the previous cases, the scaling is very good and the extracted parameters very close to those of the other systems. From this example we see in these low energy reactions a very interesting source for further characterization of the phase transition, in particular for anchoring the parameters of Fisher's model to the well established  $T = 0$  parameters of the liquid drop model.

In conclusion, the ISiS and EOS data, together with the low energy compound nucleus reaction contain the signature of a liquid to vapor phase transition via their strict adherence to Fisher's model. Through Fisher's scaling of the fragment yield distribution (Fig. 4), the two-phase coexistence line has been determined over a large energy/temperature interval extending up to the critical point. Fisher's formula (Eq. (11)) has been extensively tested and verified for the first time for any phys-

ical system. The critical exponents  $\tau$  and  $\sigma$  as well as the critical temperature  $T_c$ , the surface energy coefficient  $c_0$ , the enthalpy of evaporation  $\Delta H$  and the critical compressibility factor  $C_c^F$  have been extracted and found to agree with accepted values. Finally,  $p_c$  and  $\rho_c$  have also been determined, giving the first complete experimental determination of the critical point and the full phase diagram of finite neutral nuclear matter.

## ACKNOWLEDGMENTS

We thank Prof. C.M. Mader, Prof. R. Ghetti and Prof. J. Helgesson for their input and Ising model calculations. This work was supported by the US Department of Energy. We would also like to acknowledge the experimental and data reduction efforts of the ISiS and EOS collaborations, which made this analysis possible.

## REFERENCES

1. A. Coniglio and W. Klein, J. Phys. A **13**, 2775 (1980).
2. J. L. Cambier and M. Nauenberg, Phys. Rev. B **34**, 8071 (1986).
3. J. S. Wang, Physica A **161**, 249 (1989).
4. J. S. Wang and R. H. Swendsen, Physica A **167**, 565 (1990).

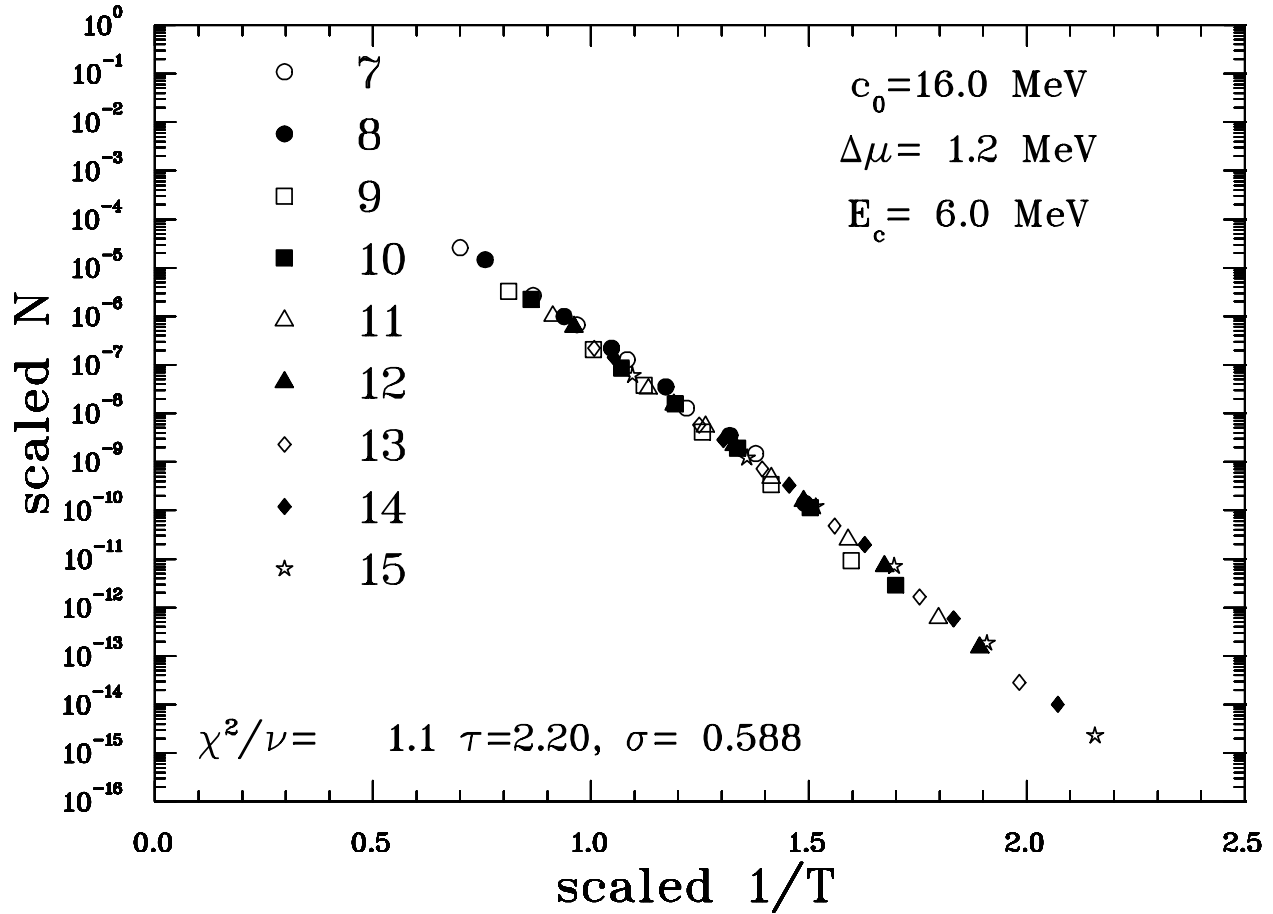


**FIGURE 12.** Preliminary results for the scaled yield distribution versus the scaled temperature for the Ni+C low energy compound nucleus decay data.

5. A. M. Ferrenberg and D. P. Landau, Phys. Rev. **B 44**, 5081 (1991).
6. A. Coniglio, Nucl. Phys. A **681**, 451c (2001).
7. F. Gulminelli and Ph. Chomaz, Phys. Rev. Lett. **82** 1402 (1999).
8. D. H. E. Gross, Phys. Rep. **279**, 119 (1997).
9. M. D'Agostino *et al.*, Phys. Lett. B, **473**, 219 (2000).
10. L. G. Moretto, *et al.*, Phys. Rep. **287**, 249 (1997).
11. L. Beaulieu *et al.*, Phys. Rev. Lett. **81**, 770 (1998).
12. L. G. Moretto *et al.*, Phys. Rev. C **60**, 031601 (1999).
13. J. B. Elliott *et al.*, Phys. Rev. Lett. **85**, 1194 (2000).
14. M. E. Fisher, Physics **3**, 255 (1967).
15. M. E. Fisher, Rep. Prog. Phys. **30**, 615 (1969).
16. C. S. Kiang and D. Stauffer, Z. Physik **235**, 130 (1970).
17. D. Stauffer and C. S. Kiang, Advances in Colloid and Interface Science **7**, 103 (1977).
18. J. B. Elliott *et al.*, Phys. Rev. Lett. **88**, 042701 (2002).
19. M.L. Gilkes *et al.*, Phys. Rev. Lett. **73**, 1590 (1994).
20. M. D'Agostino *et al.*, Nucl. Phys. A **650**, 328 (1999).
21. J.B. Elliott *et al.*, Phys. Rev. C **62**, 064603 (2000).
22. C.M. Mader *et al.*, LBNL-47575, nucl-th/0103030 (2001).
23. L. Beaulieu *et al.*, Phys. Rev. Lett. **84**, 5971 (2000).
24. L. Beaulieu *et al.*, Phys. Rev. C **63**, 031302 (2001).
25. A.H. Raduta *et al.*, Phys. Rev. C **55**, 1344 (1997).
26. K. Hagel *et al.*, Nucl. Phys. **A486**, 429 (1988).
27. K. Kwiatkowski *et al.*, NIM A360, 571 (1995).
28. T. Lefort *et al.*, Phys. Rev. Lett. **83**, 4033 (1999).
29. J. A. Hauger *et al.*, Phys. Rev. C **57**, 764 (1998).
30. J. A. Hauger *et al.*, Phys. Rev. C **62**, 024626 (2000).
31. H. R. Jaqaman *et al.*, Phys. Rev. C **27**, 2782 (1983).
32. H. R. Jaqaman *et al.*, Phys. Rev. C **29**, 2067 (1984).
33. P. Bonche *et al.*, Nucl. Phys. A **436**, 265 (1985).
34. J. N. De *et al.*, Phys. Rev. C **59**, R1 (1999).
35. J. B. Elliott *et al.*, Phys. Lett. B, **381**, 24 (1996).
36. J. B. Elliott *et al.*, Phys. Lett. B, **418**, 35 (1998).
37. E.A. Guggenheim, "Thermodynamics", 4th ed. (North-Holland, 1993).
38. E.A. Guggenheim, J. Chem. Phys., **13**, 253 (1945).
39. C. S. Kiang, Phys. Rev. Lett. **24**, 47 (1970).
40. M. E. Fisher and A. E. Ferdinand, Phys. Rev. Lett. **19**, 169 (1967).
41. D. P. Landau, Phys. Rev. B **13**, 2997 (1976).
42. T. S. Fan, *et al.*, Nucl. Phys. A **679**, 121 (2000).